Food Research International 223 (2026) 117854

Contents lists available at ScienceDirect

Food Research International

journal homepage: www.elsevier.com/locate/foodres

Tailoring anisotropy and tenderness in high-moisture extruded plant protein structures by in-line microfoaming

Hexiang Xie, Carlos Woern, Keziah Lam, Lutz Grossmann *

Department of Food Science, University of Massachusetts, 100 Holdsworth Way, Amherst, MA 01003, USA

ARTICLE INFO

Keywords:
Meat analogues
Nitrogen gas injection
Fibrous structure
Tenderization
Porosity
alternative protein
soy protein
sustainable protein
high-moisture extrusion

ABSTRACT

Meat alternatives are a sustainable food option increasingly becoming a regular part of many consumers' diets. One major challenge in developing plant-based meat alternatives is replicating the diverse range of textural characteristics found across various conventional meat products. This study investigated the impact of nitrogen gas volumetric flow rate (0, 5, 10, 20, 40 ml/min) and gas injection position (barrel section 3 (midsection) and barrel section 4 (terminal section)) on the mechanical anisotropy, textural properties, and microstructure of high moisture extrudates by modifying the porosity. The results showed that gas incorporation creates porous structures with mean pore sizes ranging from 18.18 to 73.94 μm and from 21.01 to 77.30 μm in barrel section 3 and 4, respectively. As the gas injection volume increases from 0 to 40 ml/min, the density of the extrudates was reduced up to 14.82 % while enhancing its lightness and visual fibrous structure. Moreover, the incorporated gas lowered Warner-Bratzler shear force, hardness, and chewiness in both barrel section 3 and 4 and consequently increased the tenderness of the extrudates. Similarly, the elastic anisotropy index increased from 1.35 for the control with no gas injection to 1.70 for samples with gas injection at 5 ml/min in barrel section 3. Dynamic mechanical analysis revealed a decrease in extensional storage and loss modulus as the gas flow rate increased. These findings reveal that modifying the porous structure through gas-assisted extrusion can effectively tailor the structural and textural attributes of high-moisture extrudates and indicate the potential towards more desirable product characteristics.

1. Introduction

Plant protein structures with anisotropic properties that create meat-like textures have gained considerable attention in recent years, driven by growing awareness about the environmental impact of animal-based foods and concerns regarding animal welfare (Zheng et al., 2024). A major focus in the plant-based meat alternative market is replicating the sensory attributes of traditional meat, such as texture, flavor, juiciness, and mouthfeel. Among these, achieving textural similarity to animal meat remains a significant challenge, prompting extensive research efforts to address this issue (Ozturk & Hamaker, 2023). High-moisture extrusion is a widely used technology for producing plant-based meat analogues based on its ability to create anisotropic, fibrous, meat-like structures while ensuring high versatility and throughput (Wang et al., 2022; Zink et al., 2023). Extrusion process involves the formation of a hot protein melt within the extruder barrel under high temperature, pressure, and intense shearing, which then develops into a fibrous structure in the cooling die through a combination of phase separation and shear deformation (Cornet et al., 2022). However, this process often results in a high-density, non-porous structure due to restricted water evaporation and limited expansion in the cooling die. The resulting dense structure creates a chewier texture and hinders the diffusion of flavor, pigments, and other molecules that could enhance sensory attributes. Therefore, it is essential to develop strategies that improve the microstructure of extrudates to achieve more desirable textural attributes.

Gas incorporation has been extensively studied in low-moisture extrusion to create hierarchical, ordered porous structures by increasing bubble nucleation sites in the products (Koksel & Masatcioglu, 2018). Increasing the porosity in low-moisture extrusion is positively correlated with water-holding capacity and modified textural behavior (Van Esbroeck et al., 2024). Similar observations have been made with meat protein and acrylamide gels, where it was found that increasing hydrophilic contacting surface due to larger pore diameter (decreased capillary pressure) increases the water-holding capacity and decreases the cooking loss (Stevenson et al., 2013). However, existing

* Corresponding author.
E-mail address: lkgrossmann@umass.edu (L. Grossmann).

https://doi.org/10.1016/j.foodres.2025.117854
Received 15 May 2025; Received in revised form 2 October 2025; Accepted 10 November 2025
Available online 11 November 2025

research on gas incorporation in high-moisture extrusion is limited, but has the potential to lower the density of extrudates and thereby decrease its chewiness. Nitrogen gas injection has been demonstrated to increase void fraction and porosity, which in turn enhances product lightness and tenderness (Ghanghas et al., 2024; Zink et al., 2023). In addition to direct texture modifications, porous structures may also impact post-tenderization processing, flavor distribution, and water retention (Xie & Grossmann, 2025). While gas flow rate has emerged as a key determinant of porosity, other extrusion parameters also contribute to product quality (Lorenzen et al., 2025). Moreover, further studies are needed to understand how gas incorporation affects the distribution of porous structures in extrudates, as this knowledge could enable the design of directional porous structures (Stehle et al., 2024). As summarized in Table 1, previous studies highlight a predominant focus on either pure gas flow rate or in combination with other extrusion parameters. However, the influence of gas injection position within the extruder barrel has not been addressed. This gap could be addressed by examining the combined effects of gas flow rate and injection position on the appearance, structural anisotropy, and textural properties of soy protein-based high moisture extrudates, with particular focus on tenderness.

The high-moisture extrusion process involves different processing zones within the individual barrel sections, such as mixing and melting zones, each fulfilling a specific function with specific pressure and temperature settings (Zheng et al., 2024). As the protein melt passes through these zones, it undergoes phase changes and exhibits different flow behaviors due to the superimposed pressure, shear, and temperature gradients (Li, Zhang, et al., 2024). Zhang et al. (2019) observed that the flow behavior, thermal transition, and decomposition properties of protein melts varied across processing zones. In the mixing zone, the unfolding and crosslinking of protein molecular chains in combination with the exposure of hydrophobic functional groups and the accumulation of disulfide bonds resulted in the formation of aggregate-like clusters with increased viscosity – the increased viscosity could impede the uniform incorporation of gas. Conversely, in the melting zone, the complete unfolding of protein chains led to a more flexible protein structure, which reaggregated and promoted the development of a fibrous structure – this transformation might enhance gas incorporation. Such variations are likely to impact gas diffusion and infusion behavior depending on the position at which the gas is introduced into the extruder barrel, while ultimately influencing the final properties of the product. Therefore, this study aims to develop a gas injection process to produce high-moisture extrudates with controlled porosity, pore size distribution, and tailored textural properties. The hypothesis is that increasing porosity and pore size will enhance tenderness until the pores become excessively large.

2. Materials and methods

2.1. Materials

Soy protein concentrate with a protein content of 66.1 % was donated by ADM (Chicago, IL, USA). Rhodamine B was purchased from Sigma-Aldrich Inc. (St. Louis, MO, USA). All other reagents used in this study were of reagent grade.

2.2. Methods

2.2.1. High moisture extrusion

Extrusion process. A co-rotating twin-screw extruder (Three-Tec GmbH, Seon, Switzerland) with a 40:1 L/D ratio and a 12 mm screw diameter was used, coupled with a cooling die measuring 4 × 15 × 300 mm (H × W × L). A breaker plate with a hole diameter of 3.2 mm was positioned between the barrel and the cooling die. The screw consisted of 19 elements and the screw design is displayed in Fig. 1. Processing parameters for the extrusion were selected as described previously by Stehle et al. (2024). In brief, water was fed into the barrel using a peristaltic pump to achieve a water content of 65 % in the final extrudates. Barrel sections 1 to 6 were operated at a temperature profile of 80–100–100–120–140–160 °C followed by texturization in a cooling die regulated at 40 °C using a chiller (DuraChill®, VWR, Radnor, PA, USA). The total throughput was 1 kg/h at a screw speed of 400 rpm. All extruded samples were vacuum-sealed and stored at 4 °C until further analysis.

Microfoaming. The microfoaming was performed by adding gaseous nitrogen (N_2) to the extruder barrel using specifically designed gas injection ports with an inner diameter of 4.90 mm. The gas was injected at three different positions, i.e., the inlet section (barrel 2), midsection (barrel 3), and terminal section (barrel 4) (Fig. 1). Precise control of gas addition was achieved through the use of a mass flow controller (GC1, Dakota Instruments Inc., America) at constant pressure of $p = 0.76$ MPa. With operated gas flow rates at 0, 5, 10, 20, 40 ml/min, gas-to-throughput mass fraction of 0.000 %, 0.098 %, 0.197 %, 0.395 %, 0.790 %, respectively, were achieved calculated based on the ratio of gas mass flow rate to total throughput.

Specific mechanical energy (SME). The process parameters (screw speed, screw torque, die pressure) were recorded during the process and the SME was calculated using the following Eq. (1) (Stehle et al., 2024).

$$\mathrm{SME} = \frac{2\pi n M}{\dot{m}} \tag{1}$$

where n stands for the screw speed in rpm, M stands for the screw torque in Nm, $\dot{m}$ stands for total throughput in kg/min.

2.2.2. Texture properties

Tensile test. Tensile tests were performed according to the method of Skov et al. (2024) using a texture analyzer (TA.XT Plus, Texture Technologies Corp., and Stable Micro Systems Ltd., NY, USA). Samples (15 × 15 × 4 mm) were tested in perpendicular and parallel directions at room temperature and a strain rate of 0.25 mm/s using a 5 kg load cell and serrated tensile grips (TA-96BW). The elastic anisotropic index ($AI_{Tensile}$) was also calculated using the Young's Modulus in parallel (E_{para}) and perpendicular direction (E_{per}) in accordance with Eq. (2) (Stehle et al., 2024). The Young's modulus (E) was obtained from the slope of the

Table 1
Comparison of the methodologies and measurement approaches in similar relevant studies.

Raw materials	Gas injection conditions	Other extrusion parameters	Focus	References
38.5 wt% Soy protein concentration powder, 57.7 % water, 3.8 wt% oil	Nitrogen gas fraction (0 %–0.3 wt%)	None	Extruder end-plate pressure, specific mechanical energy, perceptual lightness, textural hardness, cohesiveness, liquid absorption characteristics, porosity	(Zink et al., 2023)
30 % soy protein and 70 % water	Nitrogen gas injection pressures (GP) (0, 1 and 2.5 bar)	Cooling die temperatures (35, 50 and 65 °C)	Torque and specific mechanical energy input, density, pore size and cutting force, texture profile analysis results	(Ghanghas et al., 2024)
Ground Cagliata curd	Nitrogen gas concentration (0, 0.05, 0.10, and 0.15 % w/w)	Screw speeds (250, 300 and 350 rpm)	Process parameters porosity, proton mobility, extensibility, tensile strength, hardness	(Lorenzen et al., 2025)

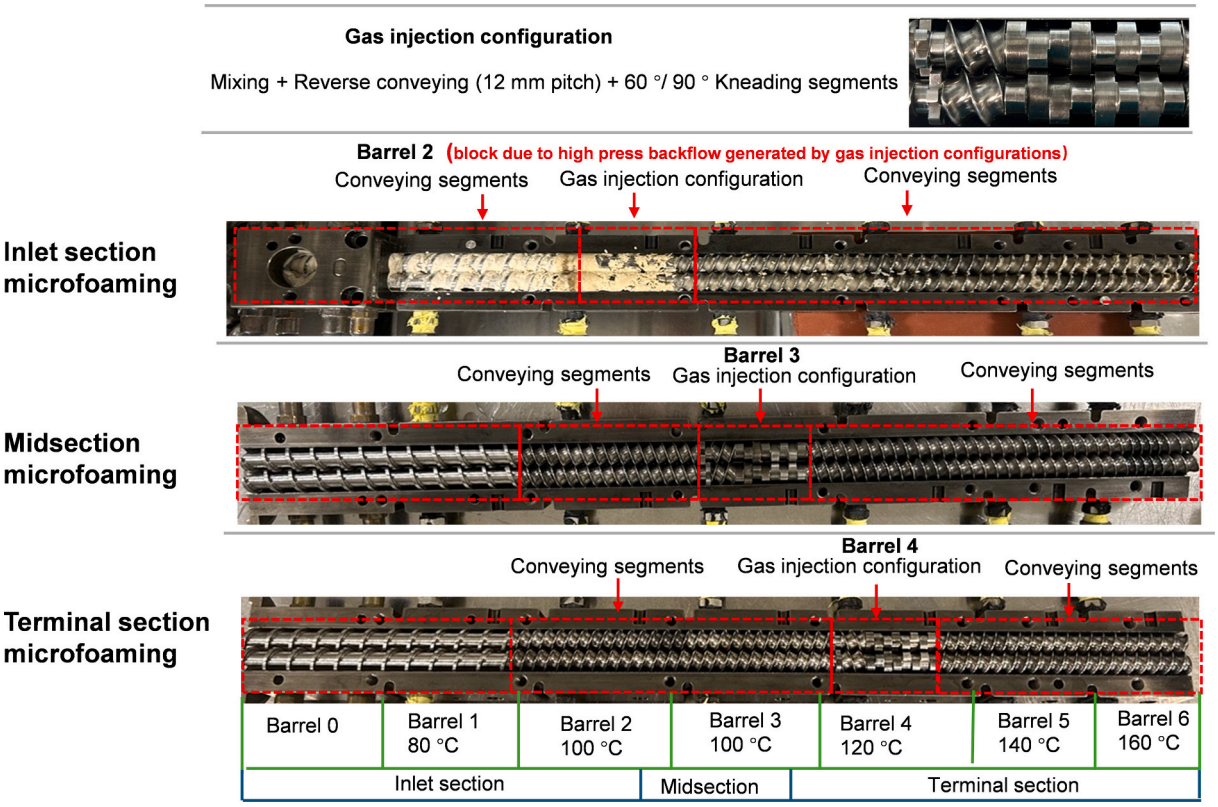

Fig. 1. Screw configuration design for the microfoaming process of soy-based high-moisture extrudates with different gas injection positions (inlet section, midsection and terminal section). The "inlet section microfoaming" process experienced a blockage caused by high-pressure backflow resulting from the gas injection configuration.

linear region of the stress-strain graph, considering strain ranges of 0.5 %–10 % for E_{para} and and 0.5 %–9 % for E_{per}.

$$AI_{Tensile} = \frac{E_{para}}{E_{per}} \quad (2)$$

Warner Bratzler shear force (WBSF). The WBSF of the extrudates (15 mm × 15 mm × 4 mm) in parallel and perpendicular direction to the protein fibers was determined using a rectangular Warner Bratzler slot blade at 1 mm/s speed and maximum displacement of 55 mm (Skov et al., 2024). The peak shear force was recorded as a function of the cutting distance. The AI_{WBSF} was obtained as the ratio of maximum WBSF in perpendicular ($WBSF_{per}$) to parallel direction ($WBSF_{para}$) as shown in Eq. (3) (Ghanghas et al., 2024).

$$AI_{WBSF} = \frac{WBSF_{per}}{WBSF_{para}} \quad (3)$$

Texture profile analysis. The extrudates (cylinder shapes, diameter 10 mm, thickness 4 mm) were tested at a travelling speed of 0.20 mm/s using a 5 kg load cell and a cylindrical probe (TA11). The measurements were conducted using a standardized double compression protocol, with a 2-s pause between strokes and a probe height of 5 mm above the sample surface after lifting (Rekola et al., 2023). The strain was set at 25 % with a trigger force of 0.05 N. The hardness, springiness, cohesiveness, and chewiness were obtained from the resulting force-distance profiles (Hu et al., 2024).

Dynamic mechanical analysis. The dynamic mechanical analysis measurements were conducted using a stress-controlled rheometer equipped with a linear lower drive (MCR702e MultiDrive, Anton Paar, Graz, Austria). An upper parallel measuring plate with a diameter of 15 mm and a lower measuring plate (L-PP25) with a diameter of 25 mm were used. The frequency sweep test was carried out for the extrudates (15 × 15 × 4 mm) at 20 °C employing a ramp of f = 0.1–100 Hz at a constant strain of γ = 0.1 % in compression mode. The initial value for proportional static force was set as 0.02 MPa with a proportional static force factor of 150 %.

2.2.3. Appearance and color

Photographs of the extrudates' surface, cross-sections (both parallel and perpendicular to the flow direction), and internal fibrous structure were taken using a digital camera (Canon Rebel T7, Tokyo, Japan) under controlled lighting conditions. A colorimeter (ColorFlex EZ 45/0-LAV, Hunter Lab, Virginia, USA) was used to quantify the color parameters (L^*, a^*, b^*) on the surfaces of the extrudates via a standardized light source (D65) and detection angle (10°). The instrument was calibrated using standardized white and black tiles.

2.2.4. Density

A pycnometer was used to measure the density of solids by applying Archimedes' principle of fluid displacement (Ghanghas et al., 2024). A 10 ml specific gravity bottle (Eisco Scientific LLC., Rochester, NY, USA) was accurately filled with water at a known density (ρ_{water}) obtained by a handheld density meter (Densito, Mettler Toledo, Switzerland) and weighed (m_1) using an analytical balance (VWR-1003 AC, VWR International, USA). Subsequently, about 1.000 g of extrudate were cut and weighed (m_2). The weighed extrudates were placed in the specific gravity bottle and then filled up with distilled water and weighed (m_3). The weight of the remaining water and specific gravity bottle was calculated as (m_3-m_2). The density of the extrudate ($\rho_{extrudate}$) was calculated from the weight of water displaced m_1-(m_3-m_2) using the following Eq. (4).

$$\rho_{extrudate} = \frac{m_2}{([m_1 - (m_3 - m_2)]/\rho_{water})} \quad (4)$$

2.2.5. Microstructure

Confocal laser scanning microscopy (CLSM) was used to visualize the microstructure of the samples. Extrudates were sliced in parallel and perpendicular direction to the flow into 30 μm thick samples at −20 °C using a cryo-microtome (Leica CM1860 Cryostat, Leica Biosystems company, Danvers, MA) with prior rapid freezing in liquid nitrogen. The extrudate slices were treated with Rhodamine B (0.1 %, 30 μl) on a microscope slide. Images were obtained using a CLSM (Nikon Eclipse C1 80i, Nikon Instruments Inc., NY, USA) equipped with a TRITC laser at 561 nm.

2.2.6. Pore size distribution and porosity

The porosity and pore size of the extrudates were analyzed in situ using a 3D X-ray microscope (Bruker Skyscan 1276 micro-CT, Bruker, Billerica, USA). The extrudates (15 × 8 × 4 mm) were individually wrapped using plastic wrap and put inside the rotating container using transparent tape. The machine was equipped with an X-ray source emitting at 80 kV and 200 μA that was used without a filter to obtain the images. Images were taken at a rotation step of 0.4°, frame averaging of 4 with a 410 ms exposure time at each angle to obtain a 3D model of the extrudates with 1920 × 2016 pixels at a resolution of 9 μm/pixel (Chanvrier et al., 2015; Luo et al., 2020). The images were reconstructed using NRecon software. Regions of interest within the cross-sectional images were identified and selected. A binary image comprising 256 Gy levels was segmented using an automatic process to determine the threshold value. The number-based histogram of size distribution was calculated for a volume of interest using the CTAN software (Bruker, Billerica, USA). The 3-D analysis was conducted to determine the volume-based three-dimensional pore size distribution, mean pore size, and total porosity. Morphometric analysis tools were employed to identify pores, which were characterized as black voxels enclosed by white voxels within the dataset. The mean pore diameter is determined by the structure thickness, which corresponds to the diameter of the black pores, using a greyscale threshold value of 75. Subsequently, a 3-D model was generated using CTAN software and further processed in CTVOL software (Bruker, Billerica, USA) to create a 3-D visualization of the extrudates.

2.2.7. Statistical analysis

All experiments were performed at least twice from fresh raw materials, and measurements were carried out at least in duplicate. Data was analyzed by one-way analysis of variance (ANOVA) with a Tukey's test ($p < 0.05$) using Origin Pro (OriginLab Corp., Northampton, MA, USA).

3. Results and discussion

Porosity is a key structural parameter that influences the quality characteristics of many foods by affecting their deformation behavior, appearance, liquid absorption and retention, and diffusion properties (Aghajanzadeh et al., 2024). Standard high-moisture extrusion does not allow the protein melt to expand due to spatial restriction within the cooling die, which prevents vapor expansion (Schmid et al., 2022). As a result, the final product is generally dense with minimal porous structures. This dense nature can have certain drawbacks, such as a firm texture, reduced lightness, and limited liquid absorption during marination, which could improve the flavor profile. For this reason, an in-line microfoaming approach was designed to enable the tailoring of the porous structure by modifying the injection location and the gas volume flow rate Q.

Initially, the screw design was optimized to facilitate the successful injection of gas and prevent any backflow of the gas mixture. To achieve this, a "gas-injection segment" was added in the screw configuration right before the gas injection port consisting of mixing, reverse, and 60°/90° kneading segments (Fig. 1). This segment was strategically positioned at three different gas injection points: the inlet section (barrel 2), the midsection (barrel 3), and the terminal section (barrel 4). However, when gas was injected into the inlet section, a blockage occurred, likely due to the high-pressure backflow of the gas caused by the protein melt not being fully developed in the initial stages causing a compression of powder particles (Fig. 1). For this reason, gas was only injected in the midsection and terminal section using different flow rates up to 40 ml/min controlled by a mass flow controller, which resulted in a successful and stable extrusion process.

3.1. Process parameters

The initial investigation focused on changes in extrusion process parameters under different microfoaming conditions. For this purpose, the SME was calculated, and the die pressure was recorded as shown in Fig. 2. No significant differences in SME were observed between the extrudates under varying microfoaming conditions. However, an increase in SME was noted for the process of the gas-injected extrudates compared to those without gas injection. Similarly, die pressure also increased for the process of gas-injected extrudates compared to those without gas injection. Specifically, the SME increased from 367.2 ± 27.9 to 445.1 ± 4.8 kJ/kg in the midsection and from 368.9 ± 5.8 to 460.4 ± 8.5 kJ/kg in the terminal section as the flow rate increased from 0 to 40 ml/min. The die pressure rose from 0.82 ± 0.01 to 1.43 ± 0.03 MPa in the midsection and from 0.87 ± 0.03 to 1.44 ± 0.02 MPa in the terminal section as the flow rate increased from 0 to 40 ml/min. Notably, at lower gas flow rates of 5 and 10 ml/min, the die pressure in the midsection was higher than that in the terminal section. The increase in SME and die pressure during in-line microfoaming can be attributed to the incorporation of gas into the protein melt. The overall higher volume of protein melt plus incorporated gas phase elevated the barrel filling degree and consequently increased the friction between screw and protein melt, while decreasing the molecular mobility. As a result, the pressure buildup intensified, which required more mechanical energy input for the protein melts to move forward. A similar increase in pressure following gas injection at concentrations up to 0.2 wt% was also observed in the study by Zink et al. (2023).

3.2. Effect on internal structure

Microfoaming was utilized to test the hypothesis of modifying the internal structure in a plant-protein matrix through the creation of a porous network. For this reason, the density, pore size distribution, and internal microstructure were analyzed. The impact of the gas-injection position in the extruder barrel and varying flow rates on the density of the high moisture extrudates are shown in Fig. 3. Extrudate densities ranging from 989.32 ± 2.97 (40 ml/min) to 1084.22 ± 10.54 kg/m^3 (0 ml/min) and from 962.56 ± 4.21 (40 ml/min) to 1130.01 ± 25.94 kg/m^3 (0 ml/min) were determined for gas injection in the midsection and in the terminal section, respectively. This aligns with the findings reported by Ghanghas et al. (2024) for gas-injected meat alternatives, who reported a decrease in density from 1,111 to 1,070 kg/m^3 as gas pressure increased from 0 to 2.5 bar. With an increasing injection flow rate, the density of the extrudates expectedly decreased as the gas injection leads to pore formation and potential product expansion after exiting the cooling die. Interestingly, a higher density was observed when lower flow rates were injected in the terminal section in comparison to the midsection; however, the opposite trend was noted at higher gas flow rates (>20 ml/min). These findings align with the study by Paulik et al. (2021), which concluded that the gas volume fraction in dough led to a significantly higher specific bread volume. Li et al. (2019) also found a decrease in the density of wheat flour extrudates as nitrogen injection pressure increased. Overall, gas injection decreased the density by up to 14.82 %, which may have important consequences on the microstructure.

Fig. 4 displays the microstructure obtained by CLSM of extruded samples cut both perpendicular and parallel to the fiber direction. The

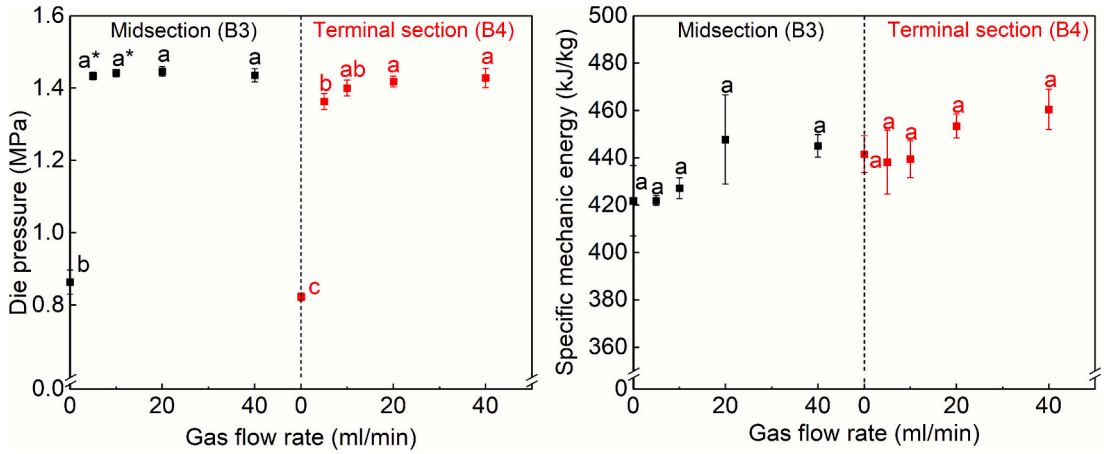

Fig. 2. SME and die pressure of high moisture extrusion processes microfoamed using different gas injection positions (midsection and terminal microfoaming) and gas flow rates. Bars with different lowercase letters show significant differences between gas flow rates at the same injection position, while * indicates differences between injection positions at the same flow rate ($p < 0.05$).

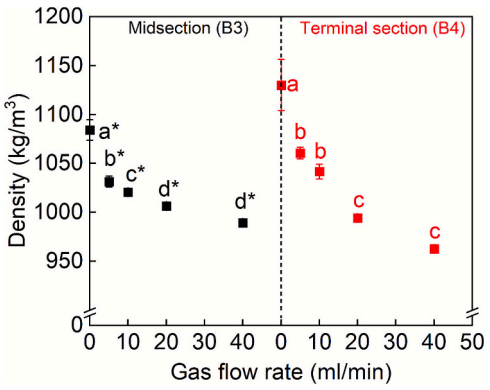

Fig. 3. Density of high moisture extrudates microfoamed using different gas injection positions (midsection and terminal microfoaming) and gas flow rates. Bars with different lowercase letters show significant differences between gas flow rates at the same injection position, while * indicates differences between injection positions at the same flow rate ($p < 0.05$).

images show that non-microfoaming results in an internal structure which is primarily composed of very dense protein layers with only a minimal number of pores. Some of these pores likely formed due to the barrel not being completely filled – a phenomenon also observed by Wang et al. (2023), who reported numerous voids in high-moisture soy protein–gluten extrudates without gas injection. In contrast, the microfoamed extrudates exhibited numerous visible pores on both the perpendicular and parallel cut cross-sectional areas. As the gas flow rate increases, more pores developed that were larger in size. This indicates that higher gas flow rates result in more nitrogen gas being incorporated into the extrudates. Especially at higher flow rates (20 and 40 ml/min), the gas injection in the terminal section resulted in more visible pores with more irregular and elongated shapes compared to pores from midsection microfoaming. This is consistent with the more fibrous structure observed in their appearance, as discussed later (see section 3.3).

The underlying reason for this observation could be the difference in barrel temperature and, consequently, product temperature. The barrel temperature in the midsection was 100 °C, whereas in the terminal section 120 °C was reached. Under the high temperature conditions, the proteins in the soy-based formulations denature and form a viscoelastic network that can entrap gas. The successful incorporation of the gas depends on two main factors. First, the gas needs to be incorporated into the protein melt, requiring the formation of a flowable mass. Second, the gas must be retained within the protein melt by developing a viscoelastic network. It is likely that more gas is retained when injected in the terminal section due to the formation of a more pronounced viscoelastic network at higher temperatures compared to the earlier sections. In addition, the injection in the terminal section reduced the exposure of the embedded gas pores to the intense shearing process, which can compress the pores (Sun et al., 2022). These two factors can simultaneously contribute to the differences in gas incorporation into the protein melt.

The microstructure observed through CLSM was also validated by micro-CT imaging. From this data, the pore size distribution was analyzed and the mean pore size and porosity were calculated (Fig. 5). The volume-based mean pore size increased from 18.18 (0 ml/min) to 73.93 μm (40 ml/min) in the midsection and from 21.01 (0 ml/min) to 77.29 μm (40 ml/min) in the terminal section. The porosity increased from 2.14 % (0 ml/min) to 9.35 % (40 ml/min) in the midsection and from 2.01 % (0 ml/min) to 15.33 % (40 ml/min) in the terminal section. This is further confirmed through 3-D model images of the soy-based high moisture extrudates with midsection foaming and terminal section foaming (Figs. 6 and S1). Lorenzen et al. (2025) also observed that increasing nitrogen concentration led to greater porosity in microfoamed casein-based extrudates. With increasing gas flow rate, the fraction of larger pores became more prominent while the proportion of smaller pores decreased. Specifically, the small pore size class (9.09 to 45.46 μm) comprised 63.6 % of all pores at a flow rate of 5 ml/min, which decreased to 40.4 % when the flow rate was increased to 40 ml/min in the midsection and from 62.8 % to 34.0 % in the terminal section. This aligns with the number-based pore size distribution shown in Fig. 5. As the flow rate increased from 0 to 40 ml/min, the percentage of pores in the size range of 18.2–72.7 μm declined from 67.9 % to 50.9 % in the midsection and from 59.7 % to 47.9 % in the terminal section. This indicates that smaller pores decreased more significantly when the microfoaming was carried out in the terminal section compared to the midsection as already indicated in the density measurements (Fig. 3). Additionally, the proportion of pores in the same pore size class was higher in the midsection compared to the terminal section at the same flow rate, which indicates that microfoaming in the midsection has a higher proportion of pores with smaller sizes. Overall, microfoaming in the terminal section produced extrudates with larger pore sizes, as reflected by the higher mean particle diameters (Fig. 5). This suggests that along with increased flow rates gas injection in the terminal section tends to generate larger pores during the extrusion process.

Overall, these results suggest that higher flow rates increase porosity, leading to lower density and larger pores, while injecting gas into the terminal section of the barrel also results in the formation of larger

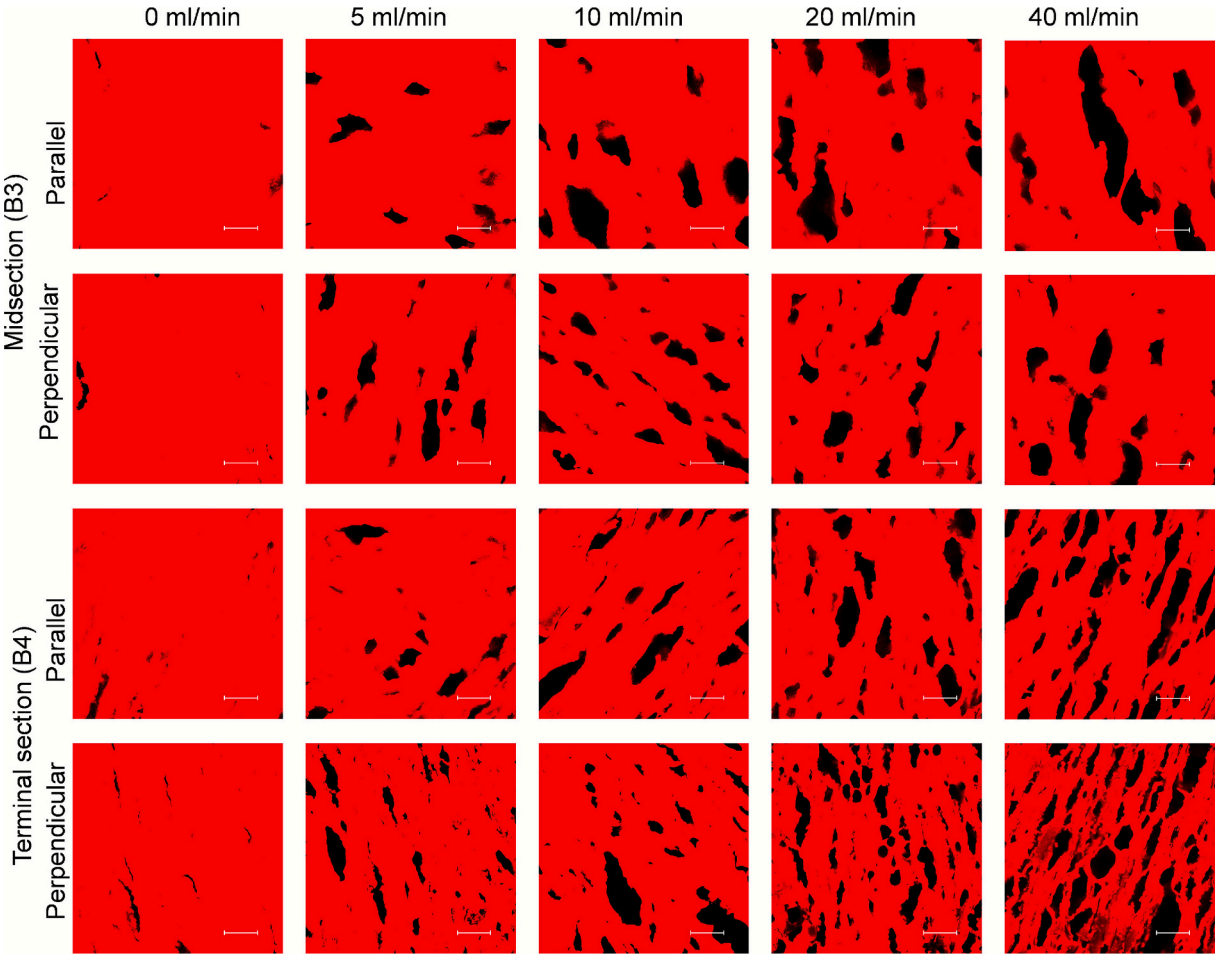

Fig. 4. Microstructure of soy-based high-moisture extrudates microfoamed at different gas injection positions (midsection and terminal) and gas flow rates, observed via confocal laser scanning microscopy sliced parallel and perpendicular to the fiber direction. The scale bar is 100 μm.

pores.

3.3. Effect on external appearance

The formation of pores alters the scattering pattern when light strikes the sample surface (Yu et al., 2023). Therefore, the microfoaming process was expected to change the color appearance of the extrudates, and Fig. 7 shows the color parameters (L^*, a^*, b^*) of the extrudates. In general, the color of the high moisture extrudates was influenced by the gas flow rate. As the gas flow rate increased from 0 to 40 ml/min, the L^* value increased, while the a^* value showed a decreasing trend. This indicates that the lightness of the extrudates increased, and they became less red. The increased lightness could be related to the formation of pores created by the injected gas, which results in a porous surface that scatters more light (Koksel & Masatcioglu, 2018). Principally, surfaces exhibit greater whiteness when more light is scattered. Porous structures with a high degree of porosity enhance the light reflectance, resulting in increased whiteness (Penttilä & Lumme, 2009). Moreover, the b^*-values increased with higher flow rates, indicating that the extrudates became more yellowish at these elevated flow rates. This is in accordance with the study of Li et al. (2019), where nitrogen gas injected wheat flour extrudates exhibited less red and brighter color as gas pressure increased. However, at higher flow rates (20 and 40 ml/min), microfoaming in the terminal section resulted in higher L^*-values and lower a^* as well as lower b^*-values compared to microfoaming in the midsection at the same flow rates. This was in accordance with the lower density (Fig. 3) and higher porosity (Fig. 5) that led to higher light reflection on the surface.

The color values were also confirmed by the visual appearance of the extrudates, which are displayed in Fig. 8A and B. The surface appearance showed that as the flow rate increased, the extrudates became whiter, developed a more fibrous structure, and displayed more prominent striations caused by the breaker plate. A similar increase in whiteness was also reported by Koksel and Masatcioglu (2018) and was related to yellow pea puffed snacks using nitrogen-assisted extrusion cooking. Moreover, microfoaming significantly affected the visual fibrosity, likely due to gas entrapment, which caused the spatial separation of individual parallel protein fibers and subsequently increased fibrosity. As the flow rate increased, the microstructures became more aligned with the flow direction and displayed thinner, more entangled, and intertwined fibers, particularly for those perpendicular to the fiber direction, which also appeared whiter. When comparing the microfoaming site, terminal microfoaming appeared to result in a whiter surface, consistent with higher L^* values (Fig. 7). Additionally, terminal microfoaming exhibited a more visual fibrous structure, indicating a more spatial separation of the protein fibers by the injected gas. This aligns with the higher porosity observed for terminal microfoaming and highlights that the terminal injection could lead to improved visual and textural properties compared to midsection microfoaming.

3.4. Effect on directional texture attributes

The visual appearance suggested a modification in textural and anisotropic characteristics caused by the microfoaming. Hence, the change in texture parameters was analyzed using texture profile analysis, tensile as well as cutting tests, and dynamic mechanical frequency

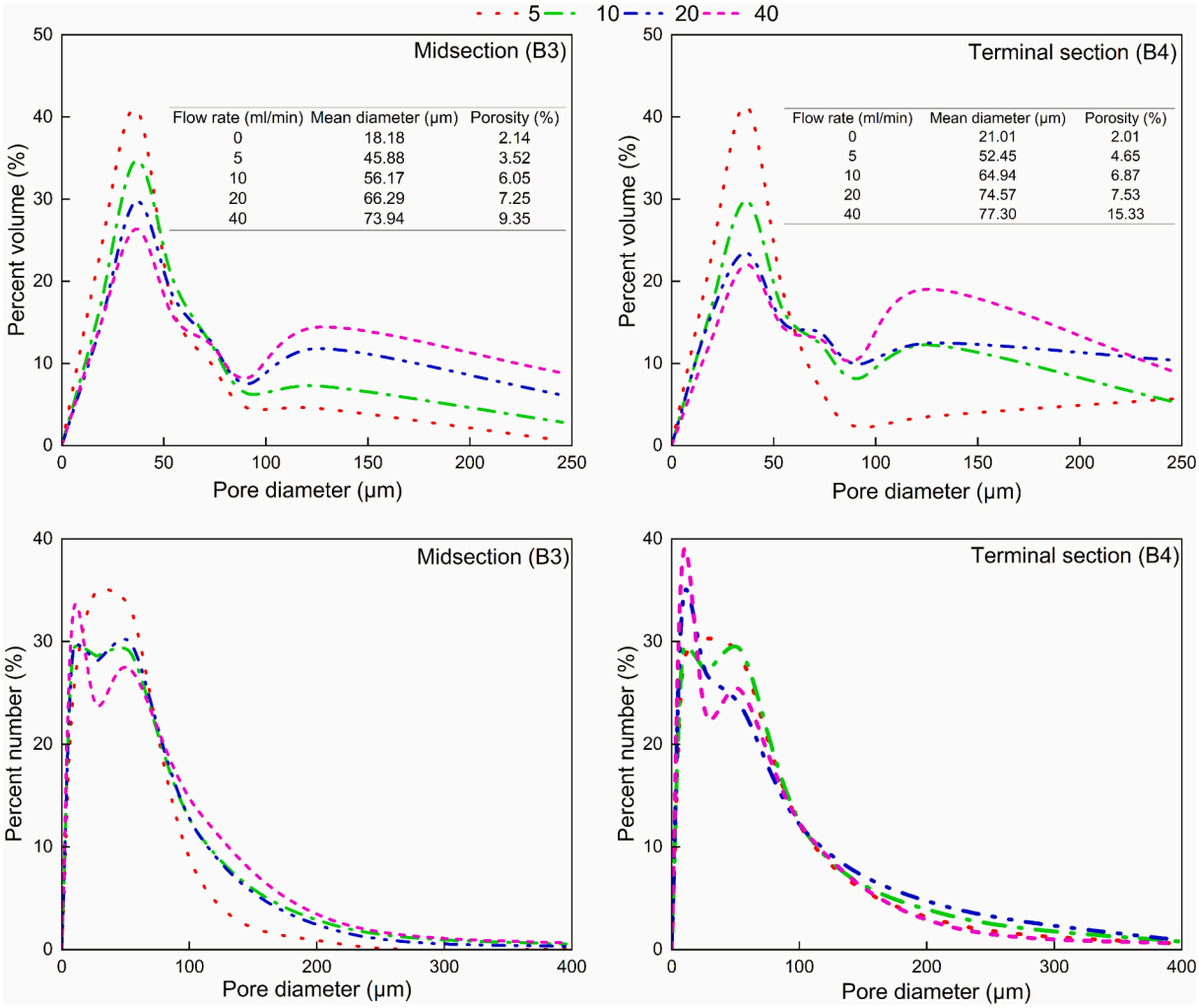

Fig. 5. Volume-based pore size distribution, volume-based mean diameter, porosity, and number-based pore size distribution of high moisture extrudates microfoamed using different gas injection positions (midsection and terminal microfoaming) and gas flow rates.

sweeps. Table 2 displays the texture profile analysis results of the extrudates. The chewiness and hardness showed a decreasing trend as the gas flow rate increased from 0 to 40 ml/min. Hardness and chewiness decreased from 17.06 ± 0.46 to 10.81 ± 0.30 N and from 12.32 ± 0.43 to 7.83 ± 0.16 N for midsection microfoaming, respectively. Similar observations were made when terminal microfoaming was employed, which lowered hardness from 19.49 ± 0.84 to 14.32 ± 0.12 N and chewiness from 14.05 ± 0.75 to 10.31 ± 0.10 N. This indicates that a higher gas flow rate results in lower hardness and chewiness, leading to a more tender texture of the extrudates. Similar phenomena were also observed by Ghanghas et al. (2024), and they found that soy protein-based high moisture extrudates subjected to nitrogen incorporation at a pressure of 2.5 bar exhibited lower hardness and chewiness values than those processed at 0 bar. Lorenzen et al. (2025) further reported that nitrogen gas injection reduced the hardness of casein-based meat analogues. The reduction in hardness and chewiness is likely due to the disruption of the microstructure (Fig. 4), which leads to a less dense protein arrangement by breaking the protein-protein network through the formation of aerated structures (Mehta et al., 2009).

Interestingly, midsection microfoaming led to a lower chewiness and hardness compared to terminal microfoaming, except at a flow rate of 10 ml/min. The elevated initial hardness and chewiness observed for the terminal section microfoaming configuration at a gas flow rate of 0 ml/min may be attributed to a more homogenous protein melt, facilitated by the kneading and mixing elements positioned closer to the cooling die. This enhanced uniformity likely promotes a denser protein structure, resulting in greater hardness and chewiness. A denser protein network formed when increased air incorporation compresses the protein melt at constant throughput in the extruder when the gas injection location is moved from the midsection to the terminal section. The lower density and more porous structure with total porosity of up to 15.33 % (Fig. 5) caused by terminal microfoaming suggests that more air is successfully introduced compared to midsection microfoaming. On the one hand, this elevated air incorporation can promote compression of the protein matrix, slightly increasing hardness and chewiness. On the other hand, the formation of more air pores within the extrudates tends to reduce these textural parameters. This dual effect aligns with the observed decrease in hardness and chewiness as gas flow rate increases at constant injection position. However, despite further gas incorporation in the terminal section, which was indicated by increased surface lightness and porosity, the chewiness and hardness remained higher than for midsection microfoaming. This indicates that the position of microfoaming plays a dominant role in melt compression and texture, outweighing the softening effect of slightly increased air incorporation. Lastly, only small changes were observed in springiness and cohesiveness values upon gas incorporation with springiness increasing from 79.91 %–84.16 % for midsection microfoaming and from 81.68 %–84.59 % for terminal microfoaming (Table 2).

When compression was carried out in oscillation mode, a similar pattern was observed as shown in Fig. 9. All the extrudates were

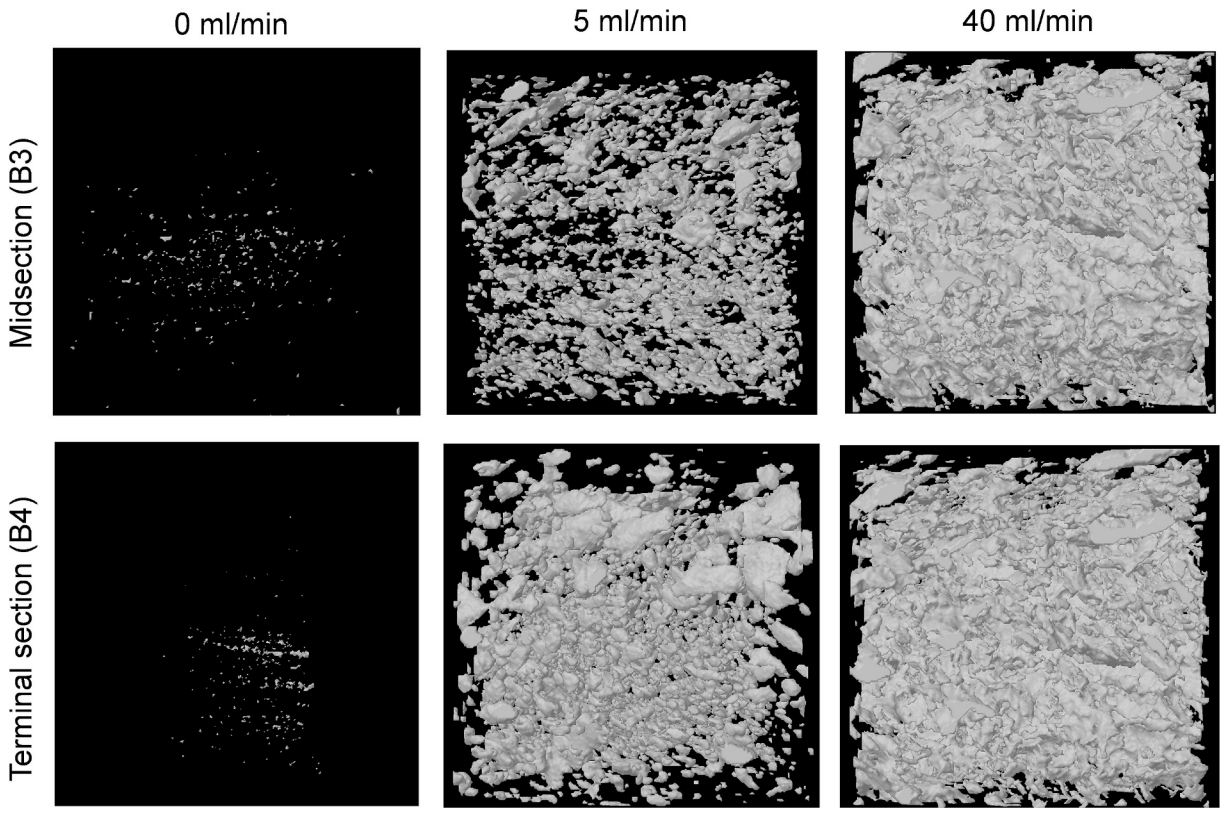

Fig. 6. Three-dimensional visualization of pore distribution of high moisture extrudates microfoamed using different gas injection positions (midsection and terminal microfoaming) and gas flow rates.

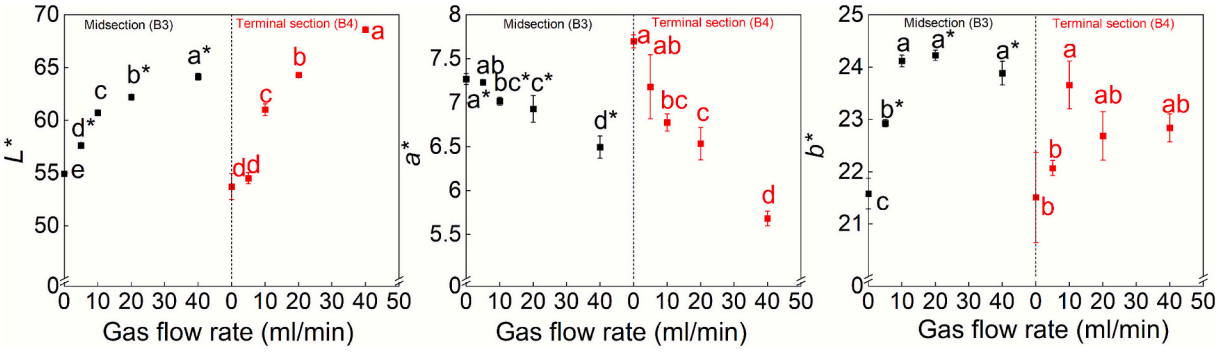

Fig. 7. Color parameters of high moisture extrudates microfoamed using different gas injection positions (midsection and terminal microfoaming) and gas flow rates. Bars with different lowercase letters show significant differences between gas flow rates at the same injection position, while ** indicate differences between injection positions at the same flow rate ($p < 0.05$).

predominantly elastic with G′ being greater than G″. Both G′ and G″ increased gradually as the frequency increased. This trend was observed in another study as well and was likely caused by the failure of extrudates to alleviate internal stresses at high frequencies, leading to material hardening (Liu et al., 2024). As the gas flow rate increased from 0 to 40 ml/min, both G′ and G″ of the extrudates decreased, which aligns with the observed decrease in hardness and similar findings were observed when normal force was applied during cutting tests (Fig. 10). A decreasing trend in the shear force for cutting both perpendicular and parallel to the fiber direction was seen with increasing gas flow rate. As the gas flow rate increased from 5 to 40 ml/min, the cutting shear force in the parallel direction decreased from 19.56 ± 0.85 to 11.92 ± 0.36 N for midsection foaming and from 20.30 ± 0.28 to 12.29 ± 0.65 N for terminal foaming. A similar trend was observed in perpendicular direction for both microfoaming positions in the extruder barrel. The reduction in cutting shear force was likely due to air pockets, which created less resistance to the cutting motion and led to extrudates with lower cutting strength (Li, Janssen, et al., 2024). Additionally, there was no significant difference ($p < 0.05$) in the cutting shear force of gas-injected extrudates in either direction between the midsection and terminal microfoaming. A similar trend was also found in the study of Ghanghas et al. (2024), where the cutting force in both directions of soy-based extrudates decreased at a gas injection pressure of 1 bar compared to the soy-based extrudates without gas injection.

Interestingly, the opposite trend was observed in tensile tests (Fig. 11). There was an increasing trend in Young's modulus both parallel and perpendicular to the flow direction as the gas flow rate increased, which is different from the results obtained in the cutting tests that showed a decreasing trend (Fig. 10). This can be attributed to the direction of the applied force and the varying modes of tension and

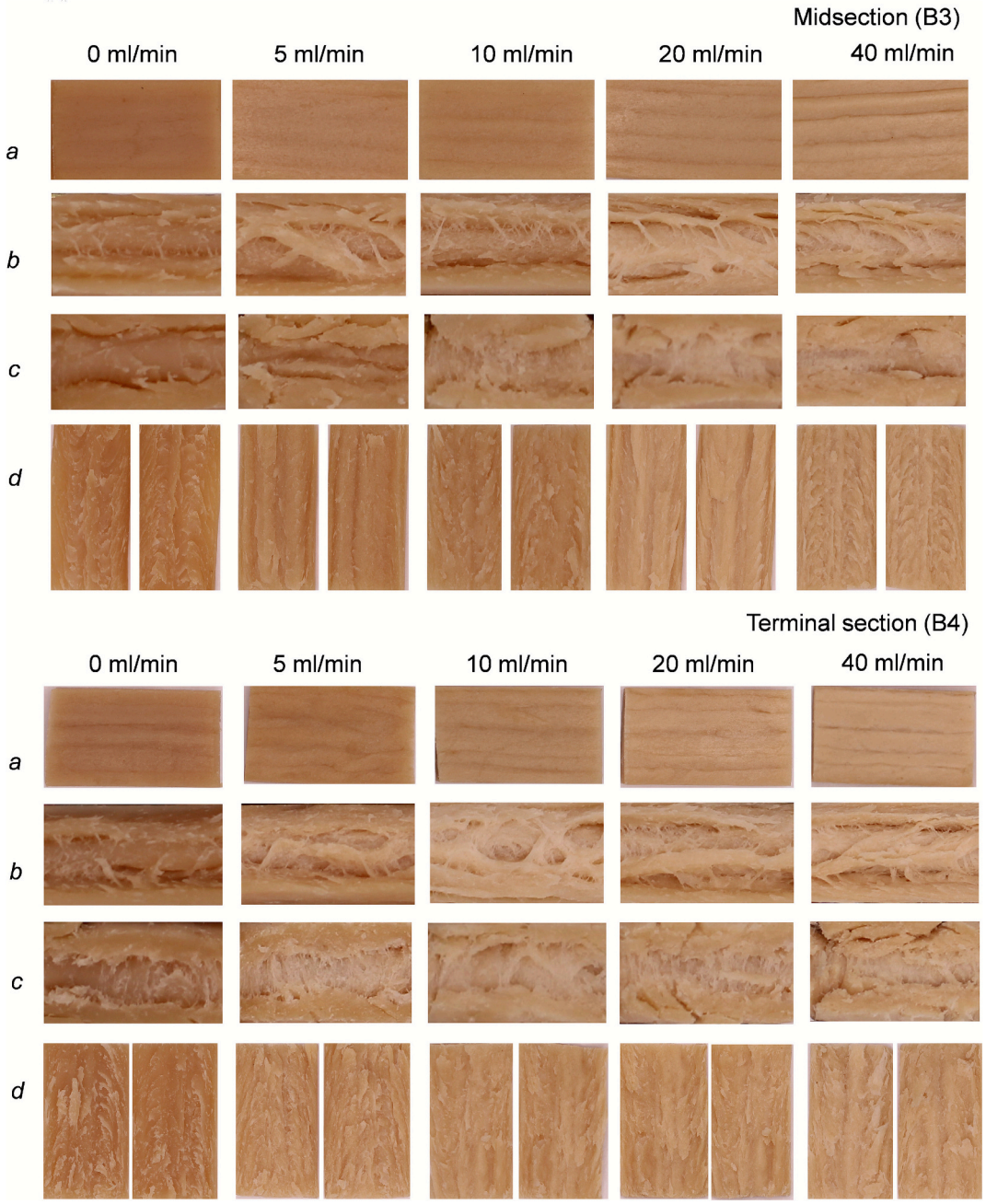

Fig. 8. The surfaces (*a*), sectioned cross-section surfaces parallel and perpendicular to the flow direction (*b* & *c*), and the internal fibrous structure (*d*) of high moisture extrudates microfoamed using different gas injection positions (midsection (top) and terminal microfoaming (bottom)) and gas flow rates.

compression, as discussed in the next section 3.5. The increased Young's modulus is caused by the formation of a more interlocked structure, leading to higher resistance to extension (Taghian Dinani et al., 2023). An increase in gas flow, increases the gas incorporation into the melt that leads to a more uniform gas distribution throughout the protein matrix. This not only improves barrel filling but also promotes separation of the protein melt into distinct layers, which increases resistance in the parallel direction and in the perpendicular direction at higher flow rates due to melt compression. The Young's modulus in parallel direction increased significantly when the gas flow rate increased to 10 ml/min for midsection and terminal microfoaming compared to the extrudates at flow rates of 0 and 5 ml/min. In contrast, microfoaming initially resulted in a decrease in the Young's Modulus in perpendicular direction at a flow rate of 5 ml/min compared to the non-foamed extrudate. At low gas flow rates, the incorporated gas likely causes separation of the protein melt with only minimal melt compression. This initially drives the formation of parallel layers in the protein melt, reducing resistance to perpendicular extension. However, as the flow rate increased to 20 ml/min, the Young's Modulus in the perpendicular direction became higher than that of the non-foamed extrudate.

The resulting forces and moduli were used to calculate the respective anisotropy indices (Eqs. (2) and (3)), which are presented in Figs. 10 and 11, respectively. The anisotropy index based on the cutting shear force increased from 1.53 to 1.65 for the midsection and from 1.59 to 1.62 for the terminal microfoaming as the flow rate increased from 0 to 5 ml/min (Fig. 10). At a flow rate of 40 ml/min, terminal microfoaming exhibited a lower anisotropy index compared to the extrudates without microfoaming. In contrast, midsection foaming showed a higher anisotropy index than terminal microfoaming at the same flow rate of 40 ml/min. A slight decrease in fibrosity is probably due to increased cross-linking of

Table 2
Texture profile analysis results (hardness, chewiness, springiness, and cohesiveness) of high moisture extrudates microfoamed using different gas injection positions (midsection and terminal microfoaming) and gas flow rates.

	Flow rate (ml/min)	Hardness (N)	Chewiness (N)	Springiness (%)	Cohesiveness
Midsection (B3)	0	17.06 ± 0.46^{a*}	12.32 ± 0.43^{a*}	84.16 ± 1.65^{a}	0.85 ± 0.00^{b}
	5	14.56 ± 0.31^{b*}	10.68 ± 0.34^{b*}	82.20 ± 1.14^{ab}	0.89 ± 0.00^{a}
	10	13.76 ± 0.26^{b}	9.75 ± 0.51^{b}	83.30 ± 0.69^{a}	0.87 ± 0.01^{b}
	20	11.71 ± 0.18^{c*}	8.14 ± 0.20^{c*}	79.91 ± 0.81^{b}	0.86 ± 0.01^{b}
	40	10.81 ± 0.30^{d*}	7.83 ± 0.16^{c*}	83.02 ± 0.71^{a}	0.87 ± 0.00^{b}
Terminal section (B4)	0	19.49 ± 0.84^{a}	14.05 ± 0.75^{a}	82.82 ± 1.37^{ab}	0.87 ± 0.00a
	5	16.83 ± 0.23^{b}	12.37 ± 0.22^{b}	84.59 ± 1.07^{a}	0.87 ± 0.00^{a*}
	10	13.84 ± 0.36^{b}	10.12 ± 1.06^{c}	83.64 ± 0.25^{ab}	0.88 ± 0.00^{a}
	20	12.41 ± 0.01^{d}	8.90 ± 0.030^{c}	81.68 ± 0.14^{b}	0.88 ± 0.00^{a}
	40	14.32 ± 0.12^{c}	10.31 ± 0.10^{c}	82.56 ± 0.10^{ab}	0.87 ± 0.00^{a}

Bars with different lowercase letters indicate significant differences between different gas flow rates at the same injection position, while bars with * indicate significant differences between different gas injection positions at the same corresponding gas flow rate.

fibers in the perpendicular direction (Sun et al., 2023). A similar trend was observed for the anisotropy index obtained through tensile tests (Fig. 11). The anisotropy index for all the extrudates was greater than 1, indicating a fibrous structure that necessitates a higher force for deformation in the parallel direction compared to the perpendicular direction (Ghanghas et al., 2024). The anisotropy index of extrudates without gas injection was 1.35 for the midsection injection screw design and 1.07 for the terminal section screw design (Fig. 1), which indicates that modifying the screw design had a considerable influence on the anisotropy even without microfoaming. The highest anisotropy indices of 1.70 and 1.65 were observed at a flow rate of 5 ml/min for midsection and terminal microfoaming, respectively. Especially midsection foaming resulted in a higher anisotropy index, which might be related to a lower interlocking network as discussed in the next paragraph. However, as the gas flow rate continued to rise from 5 to 40 ml/min, the anisotropy index showed a decrease compared to the extrudates at a gas flow rate of 5 ml/min.

The decrease in the anisotropy index does not align with the observed increase in visual fibrosity, as discussed in Section 3.3 and shown in Fig. 8 (Stehle et al., 2024). This is mainly related to a proportionally higher increase in the perpendicular tensile stress that was observed as the gas flow rate increased. This correlates with the higher degree of crosslinking between individual protein fibers in the perpendicular direction, creating a more interlocking network within the extrudates and leading to greater visible fibrosity and an increase in resistance towards perpendicular tensile deformation (Fig. 11) (Oppen et al., 2024). This lowers the ratio between the parallel and perpendicular stress, which consequently decreases the measured elastic anisotropy index.

Overall, microfoaming considerably modifies the textural attributes of extrudates obtained by high moisture extrusion with a more tender and anisotropic structure in normal force direction and an increase in tensile stress that yields maximum anisotropy at a flow rate of 5 ml/min.

3.5. Process-structure relationship

Based on the presented results, the following mechanism is proposed on how microfoaming influences the textural and anisotropic properties of high moisture extruded plant proteins. The potential mechanism of process-structure relation is shown in Fig. 12. Successful gas incorporation into the protein matrix is initially indicated by a significant increase in die pressure following gas injection. This rise in die pressure reflects a higher filling degree during extrusion because of expanded protein melt, which could also be caused by slower conveying of the melt through the barrel. It is proposed that gas injection enhances fibrosity by generating oriented micropores aligned with the longitudinal direction of the fibers. The presence of gas bubbles contributes to a more anisotropic structure within the protein phase (Wang et al., 2019). This would promote fiber alignment and entanglement of protein molecule chains. As the gas flow rate increases, more gas is incorporated along the flow direction, promoting the formation of fibrous structures aligned in parallel. The increased gas content becomes more evenly distributed throughout the protein melt, enhancing the development of an interlocked fibrous network. While encouraging visual fibrosity, gas injection also affected the textural attributes, increasing the Young's modulus and decreasing the hardness, chewiness, and shear force. The reverse phenomena observed in Young's modulus (increase) and shear force (decrease) can be attributed to the direction of the applied force and the different modes of tension and compression. As the gas flow rate increased, the fibers in both directions became more well-structured and formed a more interlocked network, resulting in an increased force

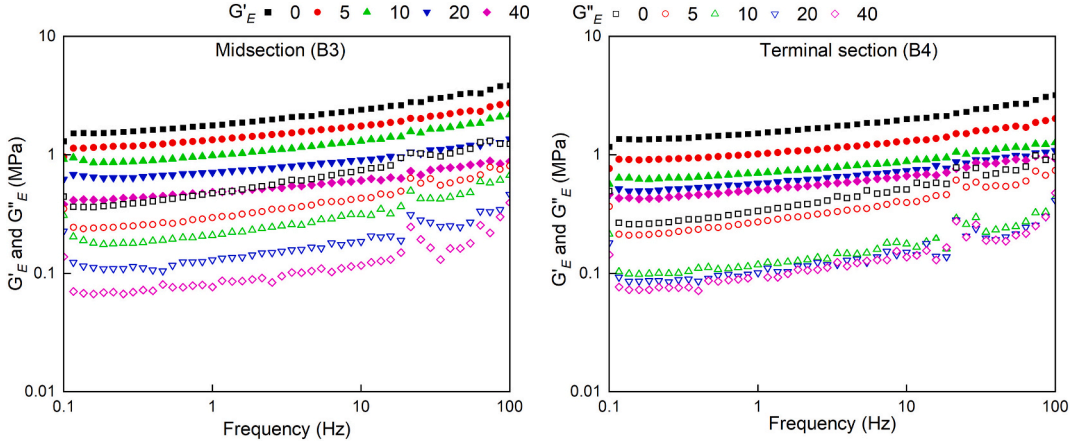

Fig. 9. Frequency sweep obtained from dynamic mechanical analysis (γ = 0.1 %) showing the extensional storage and loss modulus of high-moisture extrudates microfoamed at different gas injection positions (midsection and terminal) and gas flow rates given in ml/min.

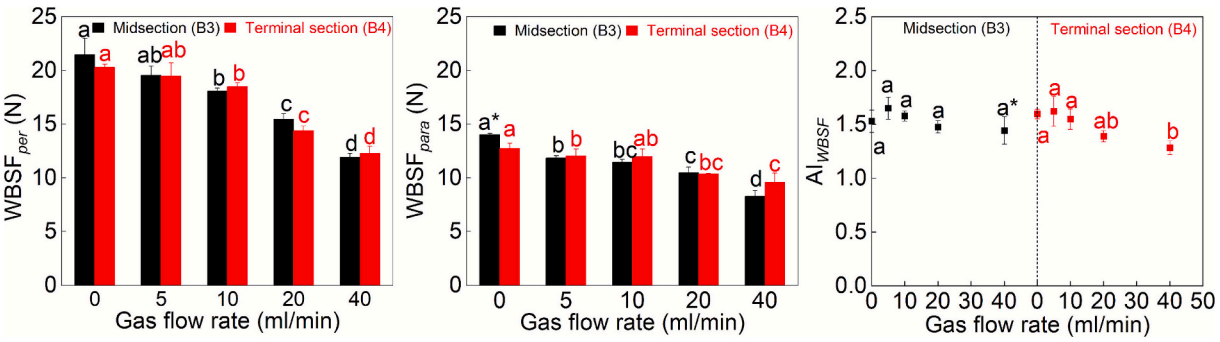

Fig. 10. Warner Brazler shear force (WBSF) measured in parallel and perpendicular direction to the fiber orientation as well as the calculated anisotropy index of high moisture extrudates microfoamed using different gas injection positions (midsection and terminal microfoaming) and gas flow rates. Bars with different lowercase letters show significant differences between gas flow rates at the same injection position, while * indicates differences between injection positions at the same flow rate ($p < 0.05$).

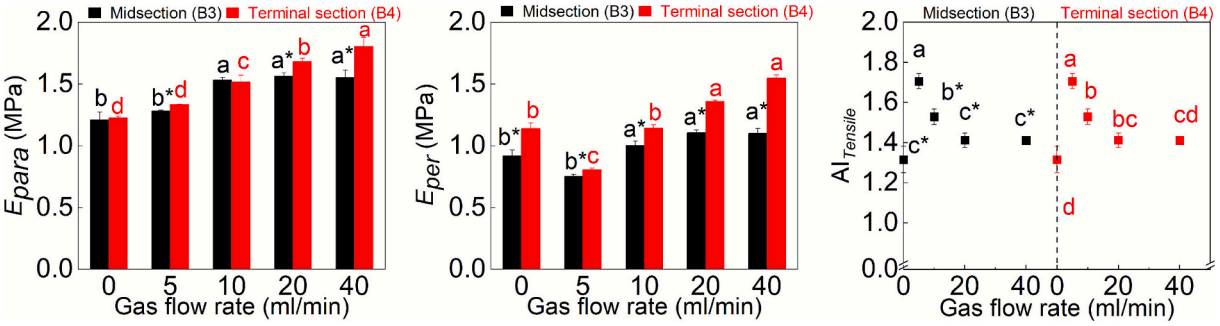

Fig. 11. Young's modulus calculated from the stress-strain correlation of extrudates tested in parallel and perpendicular direction to the fiber orientation as well as the calculated anisotropy index of high moisture extrudates microfoamed using different gas injection positions (midsection and terminal microfoaming) and gas flow rates. Bars with different lowercase letters show significant differences between gas flow rates at the same injection position, while * indicates differences between injection positions at the same flow rate ($p < 0.05$).

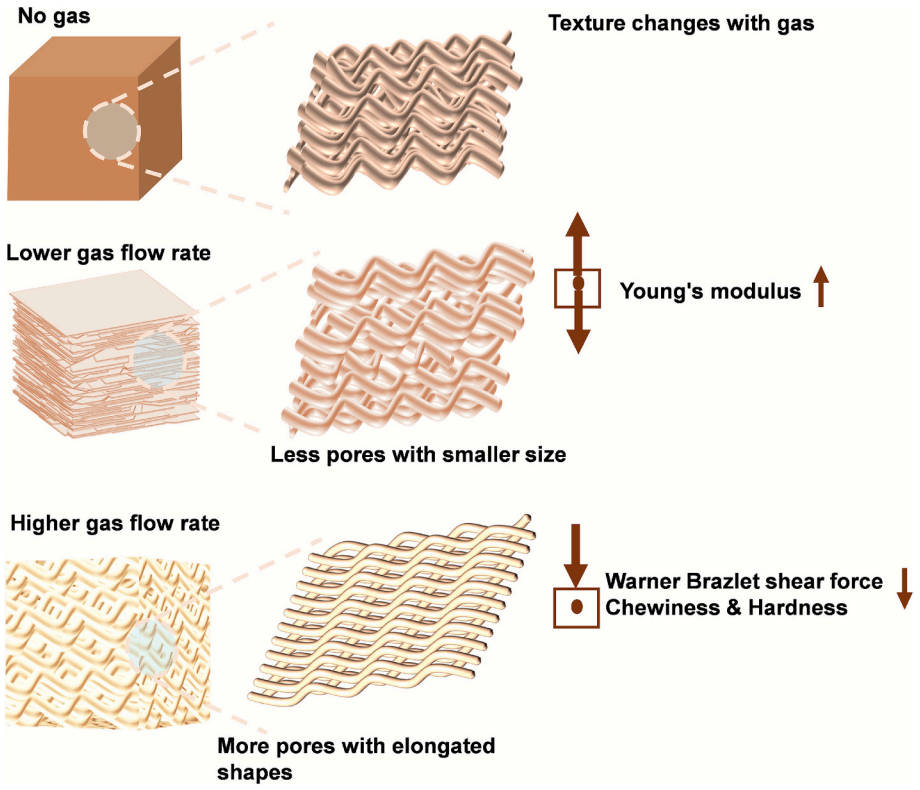

Fig. 12. Schematic mechanisms of fibrous structure formation and mechanical characteristics of microfoamed high moisture extrudates at different gas flow rates.

required to pull the extrudates, especially in the perpendicular direction. Conversely, the porous structure formed by gas injection reduces cutting and compression resistance due to the voids within the extrudates, which create weak points and facilitate easier force penetration during cutting operations.

4. Conclusion

This study revealed that microfoaming during high-moisture extrusion modifies appearance, structure, and fibrosity. Among the parameters studied, gas flow rate has a more pronounced impact on porosity and textural characteristics than the gas injection position. As the gas injection flow rate increased, extrudate density decreased, porosity increased, and the pore structure changed with increasing fraction of larger pores and decreasing proportion of smaller pores. Higher porosity and average pore size were observed in the terminal section microfoaming. Higher gas flow rates lead to higher lightness and lower chewiness, hardness, and Warner Bratzler shear force, thereby improving appearance and tenderness. Young's modulus exhibited an increasing trend in both the parallel and perpendicular directions relative to the flow as the gas injection rate rose. Gas injection enhances the fibrous structure of the extrudates, increasing the anisotropy index and creating interlocked complex network-like fibers. When comparing the microfoaming site, terminal microfoaming appeared to result in a more visual fibrous structure at higher gas flow rate. The optimal gas injection rates for achieving a tender structure were observed at a gas-to-throughput ratio of 0.79 % when microfoaming occurred in the midsection of the barrel, while the highest anisotropy was achieved at a ratio of 0.098 % when microfoaming took place in the midsection. Modulating the gas flow rate and injection position presents a promising approach to replicating the textural characteristics of different meat types, particularly those distinguished by their fibrous structure and tenderness. Moreover, it allows for the customization of the structural properties and porosity of the high-moisture extrudate, creating promising opportunities for subsequent post-processing.

CRediT authorship contribution statement

Hexiang Xie: Writing – review & editing, Writing – original draft, Methodology, Investigation, Data curation. **Carlos Woern:** Writing – review & editing, Visualization, Investigation, Data curation. **Keziah Lam:** Investigation, Data curation. **Lutz Grossmann:** Writing – review & editing, Writing – original draft, Supervision, Resources, Project administration, Funding acquisition, Conceptualization.

Funding

This work is supported by the Agriculture and Food Research Initiative - Foundational and Applied Science Program, project award no. 2023-67017-40582, from the U.S. Department of Agriculture's National Institute of Food and Agriculture. Any opinions, findings, conclusions, or recommendations expressed in this publication are those of the author(s) and should not be construed to represent any official USDA or U.S. Government determination or policy.

Declaration of competing interest

The authors declare the following financial interests/personal relationships which may be considered as potential competing interests: L. G. consults for different plant-based food companies.

Acknowledgments

The authors would like to thank the Institute for Animal Imaging facility, Institute for Applied Life Science for providing access to X-ray microscopy measurement equipment. They also thank Said Akli and James Chambers from the Animal Imaging facility for their valuable insights and discussions regarding X-ray microscopy.

Appendix A. Supplementary data

Supplementary data to this article can be found online at https://doi.org/10.1016/j.foodres.2025.117854.

Data availability

Data will be made available on request.

References

Aghajanzadeh, S., Sultana, A., Mohammad Ziaiifar, A., & Khalloufi, S. (2024). Formation of pores and bubbles and their impacts on the quality attributes of processed foods: A review. *Food Research International, 188*, Article 114494. https://doi.org/10.1016/j.foodres.2024.114494

Chanvrier, H., Nordström Pillin, C., Vandeputte, G., Haiduc, A., Leloup, V., & Gumy, J.-C. (2015). Impact of extrusion parameters on the properties of rice products: A physicochemical and X-ray tomography study. *Food Structure, 6*, 29–40. https://doi.org/10.1016/j.foostr.2015.06.004

Cornet, S. H. V., Snel, S. J. E., Schreuders, F. K. G., Van Der Sman, R. G. M., Beyrer, M., & Van Der Goot, A. J. (2022). Thermo-mechanical processing of plant proteins using shear cell and high-moisture extrusion cooking. *Critical Reviews in Food Science and Nutrition, 62*(12), 3264–3280. https://doi.org/10.1080/10408398.2020.1864618

Ghanghas, N., Nadimi, M., Paliwal, J., & Koksel, F. (2024). Gas-assisted high-moisture extrusion of soy-based meat analogues: Impacts of nitrogen pressure and cooling die temperature on density, texture and microstructure. *Innovative Food Science & Emerging Technologies, 92*, Article 103557. https://doi.org/10.1016/j.ifset.2023.103557

Hu, X., Ju, Q., Koo, C. K. W., & McClements, D. J. (2024). Influence of complex coacervation on the structure and texture of plant-based protein-polysaccharide composites. *Food Hydrocolloids, 147*, Article 109333. https://doi.org/10.1016/j.foodhyd.2023.109333

Koksel, F., & Masatcioglu, M. T. (2018). Physical properties of puffed yellow pea snacks produced by nitrogen gas assisted extrusion cooking. *LWT, 93*, 592–598. https://doi.org/10.1016/j.lwt.2018.04.011

Li, D., Zhang, T., Gao, F., Zhou, C., Sun, D., Gao, Y., & Wu, M. (2024). The study of numerical simulation and texture of soybean protein based on high moisture extrusion with different screw elements. *Innovative Food Science & Emerging Technologies, 92*, Article 103560. https://doi.org/10.1016/j.ifset.2023.103560

Li, J., Janssen, F., Verfaillie, D., Brijs, K., Delcour, J. A., Gunes, D. Z., … Wouters, A. G. B. (2024). The interplay between soy proteins and dietary fiber in determining the structure and texture of high moisture extrudates. *Food Hydrocolloids, 156*, Article 110256. https://doi.org/10.1016/j.foodhyd.2024.110256

Li, X., Masatcioglu, M. T., & Koksel, F. (2019). Physical and functional properties of wheat flour extrudates produced by nitrogen injection assisted extrusion cooking. *Journal of Cereal Science, 89*, Article 102811. https://doi.org/10.1016/j.jcs.2019.102811

Liu, X., Zhao, Y., Li, K., Shen, S., & Li, J. (2024). Exploring the mechanism of amylose/amylopectin improving formation of yeast-soy protein high-moisture extrudates based on small and large amplitude oscillatory shear rheology. *Food Hydrocolloids, 153*, Article 110062. https://doi.org/10.1016/j.foodhyd.2024.110062

Lorenzen, M., Tică, A., Van Den Berg, F. W. J., Lillevang, S. K., Windhab, E. J., & Ahrné, L. (2025). The effect of nitrogen injection on the structure and textural properties of casein-based extrudates. *Food Hydrocolloids, 164*, Article 111142. https://doi.org/10.1016/j.foodhyd.2025.111142

Luo, S., Chan, E., Masatcioglu, M. T., Erkinbaev, C., Paliwal, J., & Koksel, F. (2020). Effects of extrusion conditions and nitrogen injection on physical, mechanical, and microstructural properties of red lentil puffed snacks. *Food and Bioproducts Processing, 121*, 143–153. https://doi.org/10.1016/j.fbp.2020.02.002

Mehta, K. L., Scanlon, M. G., Sapirstein, H. D., & Page, J. H. (2009). Ultrasonic investigation of the effect of vegetable shortening and mixing time on the mechanical properties of bread dough. *Journal of Food Science, 74*(9). https://doi.org/10.1111/j.1750-3841.2009.01346.x

Oppen, D., Grossmann, L., & Weiss, J. (2024). Insights into characterizing and producing anisotropic food structures. *Critical Reviews in Food Science and Nutrition, 64*(4), 1158–1176. https://doi.org/10.1080/10408398.2022.2113365

Ozturk, O. K., & Hamaker, B. R. (2023). Texturization of plant protein-based meat alternatives: Processing, base proteins, and other constructional ingredients. *Future Foods, 8*, Article 100248. https://doi.org/10.1016/j.fufo.2023.100248

Paulik, S., Paczkowski, C., Laukemper, R., Becker, T., & Jekle, M. (2021). Texture design of gluten-free bread by mixing under controlled headspace atmosphere. *European Food Research and Technology, 247*(9), 2333–2343. https://doi.org/10.1007/s00217-021-03793-z

Penttilä, A., & Lumme, K. (2009). The effect of the properties of porous media on light scattering. *Journal of Quantitative Spectroscopy and Radiative Transfer, 110*(18), 1993–2001. https://doi.org/10.1016/j.jqsrt.2009.05.009

Rekola, S.-M., Kårlund, A., Mikkonen, S., Kolehmainen, M., Pomponio, L., & Sozer, N. (2023). Structure, texture and protein digestibility of high moisture extruded meat

alternatives enriched with cereal brans. *Applied Food Research, 3*(1), Article 100262. https://doi.org/10.1016/j.afres.2023.100262

Schmid, E., Farahnaky, A., Adhikari, B., & Torley, P. J. (2022). High moisture extrusion cooking of meat analogs: A review of mechanisms of protein texturization. *Comprehensive Reviews in Food Science and Food Safety, 21*(6), 4573–4609. https://doi.org/10.1111/1541-4337.13030

Skov, K. B., Suwal, S., Corredig, M., & Martinez, M. M. (2024). New milk protein anisotropic structures formed by high moisture extrusion. *Food Hydrocolloids, 149,* Article 109645. https://doi.org/10.1016/j.foodhyd.2023.109645

Stehle, F., Woern, C., Tan, N. K., Weiss, J., & Grossmann, L. (2024). Effect of oil–water colloidal states in liquid feeds on extrudability and textural attributes of high-moisture meat alternatives. *Sustainable Food Technology, 2*(5), 1569–1582. https://doi.org/10.1039/D4FB00096J

Stevenson, C. D., Dykstra, M. J., & Lanier, T. C. (2013). Capillary pressure as related to water holding in polyacrylamide and chicken protein gels. *Journal of Food Science, 78* (2). https://doi.org/10.1111/1750-3841.12036

Sun, D., Wu, M., Zhou, C., & Wang, B. (2022). Transformation of high moisture extrusion on pea protein isolate in melting zone during: From the aspects of the rheological property, physicochemical attributes and modification mechanism. *Food Hydrocolloids, 133*, Article 108016. https://doi.org/10.1016/j.foodhyd.2022.108016

Sun, D., Zhang, B., Zhou, C., Wang, B., & Wu, M. (2023). Study on high moisture extruded pea protein isolate based on acid-induced process: Physicochemical properties, conformational changes and fibrous structure mechanism. *Food Hydrocolloids, 141*, Article 108746. https://doi.org/10.1016/j.foodhyd.2023.108746

Taghian Dinani, S., Van Der Harst, J. P., Boom, R., & Van Der Goot, A. J. (2023). Effect of l-cysteine and l-ascorbic acid addition on properties of meat analogues. *Food Hydrocolloids, 134*, Article 108059. https://doi.org/10.1016/j.foodhyd.2022.108059

Van Esbroeck, T., Sala, G., Stieger, M., & Scholten, E. (2024). Effect of structural characteristics on functional properties of textured vegetable proteins. *Food Hydrocolloids, 149*, Article 109529. https://doi.org/10.1016/j.foodhyd.2023.109529

Wang, H., Van Den Berg, F. W. J., Zhang, W., Czaja, T. P., Zhang, L., Jespersen, B. M., & Lametsch, R. (2022). Differences in physicochemical properties of high-moisture extrudates prepared from soy and pea protein isolates. *Food Hydrocolloids, 128*, Article 107540. https://doi.org/10.1016/j.foodhyd.2022.107540

Wang, Z., Ji, Y., Fu, L., Pan, H., He, Z., Zeng, M., Qin, F., & Chen, J. (2023). Potential use of gluten hydrolysate as a plasticizer in high-moisture soy protein–gluten extrudates. *Journal of Food Engineering, 354*, Article 111565. https://doi.org/10.1016/j.jfoodeng.2023.111565

Wang, Z., Tian, B., Boom, R., & Van Der Goot, A. J. (2019). Understanding the role of air and protein phase on mechanical anisotropy of calcium caseinate fibers. *Food Research International, 121*, 862–869. https://doi.org/10.1016/j.foodres.2019.01.009

Xie, H., & Grossmann, L. (2025). Tenderness in meat and meat alternatives: Structural and processing fundamentals. *Comprehensive Reviews in Food Science and Food Safety, 24*(1), Article e70033. https://doi.org/10.1111/1541-4337.70033

Yu, S., Chen, J., Gomard, G., Hölscher, H., & Lemmer, U. (2023). Recent progress in light-scattering porous polymers and their applications. *Advanced Optical Materials, 11* (13), Article 2203134. https://doi.org/10.1002/adom.202203134

Zhang, J., Liu, L., Jiang, Y., Faisal, S., Wei, L., Cao, C., … Wang, Q. (2019). Converting peanut protein biomass waste into “double green” meat substitutes using a high-moisture extrusion process: A multiscale method to explore a process for forming a meat-like fibrous structure. *Journal of Agricultural and Food Chemistry, 67*(38), 10713–10725. https://doi.org/10.1021/acs.jafc.9b02711

Zheng, Y., Gu, Z., Sun, C., Zhao, Y., Cao, Y., Lu, W., Zhang, Y., & Fang, Y. (2024). Inducing melt elongation flow and controlling cooling temperature facilitate the texturization of high-moisture soy protein extrudates. *Food Hydrocolloids, 157*, Article 110452. https://doi.org/10.1016/j.foodhyd.2024.110452

Zink, J. I., Zeneli, L., & Windhab, E. J. (2023). Micro-foaming of plant protein based meat analogues for tailored textural properties. *Current Research in Food Science, 7*, Article 100580. https://doi.org/10.1016/j.crfs.2023.100580